

# Eight-year natural environmental exposure and sustained-loading of reinforced concrete beams with iron-based shape memory alloys

Yunus Emre Harmanci <sup>a</sup>, Christoph Czaderski <sup>a</sup>, Moslem Shahverdi <sup>a,b,\*</sup>

<sup>a</sup> Empa, Swiss Federal Laboratories for Materials Science and Technology, Dübendorf, 8600, Switzerland

<sup>b</sup> School of Civil Engineering, University of Tehran, Tehran 4563-11155, Iran

## ARTICLE INFO

### Keywords:

Iron-based shape memory alloy  
Near-surface mounted  
Strengthening  
Prestressing  
Durability  
Long-term  
Sustained loading

## ABSTRACT

Low-cost iron-based shape memory alloys (Fe-SMA) are recently proving to be favorable alternatives for strengthening reinforced concrete (RC) members. Unlike carbon fiber reinforced polymers (CFRP), Fe-SMAs eliminate the need for labor-intensive anchorages and exhibit plastic behavior similar to reinforcing steel, rendering them especially promising for prestressed near-surface mounted (NSM) applications. However, due to their recent development, not many long-term experimental studies have been yet available and thus the long-term durability of Fe-SMA-strengthened RC members remains relatively unexplored. To this end, the structural behavior of two RC beams strengthened with NSM Fe-SMA were investigated, exposed to a natural environmental conditions and sustained loading above their cracking load level for 8 years, followed by four-point bending until failure. Results were compared with a previous investigation of identical beams and Fe-SMA strips without exposure to environmental factors or sustained loading. Additionally, a comprehensive cross-section analysis (CSA) was conducted for both long-term exposure and four-point bending. Despite notable creep effects caused by the 8 years of sustained loading that accounted to approximately 55% of the total mid-span deflections, no significant differences were observed in terms of load-carrying capacity, ultimate deflections, or strains, compared to the unexposed beams. The employed CSA effectively captured the long-term and bending behavior. Additionally, a parameter study and global sensitivity analysis were conducted to identify influential parameters affecting structural performance, concrete compressive strength was found as the most dominant influencing parameter.

## 1. Introduction

Strengthening of existing reinforced concrete (RC) structures has been a major interest of owners and operators, aiming to meet current guideline load demands or increased load requirements, remedy against ageing structural systems, and extend design life in a cost-effective and sustainable alternative to rebuilding. RC members that are dominantly subjected to bending, such as slabs and beams, can be strengthened by either (i) adding material to the compression zone (e.g. ultra-high performance fiber-reinforced concrete [1]) or (ii) the tension zone. The latter has attracted considerable interest within the last three decades, with carbon fiber reinforced polymers (CFRP) having been the most prevalent choice [2]. The CFRP can be applied either as an externally bonded reinforcement (EBR), or a near-surface mounted (NSM) reinforcement. NSM strengthening offer an additional benefit of better bonding compared to EBR due to an increased perimeter-to-cross-sectional area ratio [3]. The improved bond resistance can be exploited by prestressing the CFRP [4], facilitating better utilization

of the materials high strength and greatly affecting the serviceability (e.g. deflections, cracks) [5]. It has been demonstrated by many researchers that this technique provides an enhanced static and fatigue performance [6–9]. However, NSM-CFRP requires tedious and elaborate prestressing systems, which has hindered their widespread use within the industry.

With the development of low-cost iron-based shape memory alloys (Fe-SMA) [11], the feasibility of a simplified prestressing procedure, also referred to as “activation”, emerged. This is due to the so-called “shape memory effect (SME)”, undergoing a reversible phase transformation between martensite and austenite phases, recovering its original shape after deformation upon the application of appropriate thermal stimuli. If the deformations are blocked from both ends, not allowing the material to return to its original state, a “recovery stress” is created [12–16]. The FeSMA-NSM reinforcement could be fixed at both ends of the groove by mortar and then activated through heating to generate prestressing at the free length [17], which facilitates a much

\* Corresponding author.

E-mail addresses: [moslem.shahverdi@ut.ac.ir](mailto:moslem.shahverdi@ut.ac.ir), [moslem.shahverdi@empa.ch](mailto:moslem.shahverdi@empa.ch) (M. Shahverdi).

**Table 1**  
Overview of specimens (A: activated, NA: non-activated, ST: short-term, LT: long-term).

Beam No.	Properties	Comments
Beam 1	Reference, no strengthening, ST	Denoted by gray color in the manuscript.
Beam 2	2x NA-FeSMA strips, ST	Denoted by gray color in the manuscript.
Beams 3, 4, 6	2x A-FeSMA strips, ST	Denoted by gray color in the manuscript.
Beam 5	1x CFRP strip, ST	Reported in [10], not discussed herein
Beam 7	2x A-FeSMA strips, LT	Denoted by blue color in the manuscript.
Beam 8	2x NA-FeSMA strips, LT	Denoted by red color in the manuscript.



**Fig. 1.** Fe-SMA strip (20 × 1.7 mm) after cold-forming the ribs (40/130° rib angle).

simpler prestressing procedure compared to NSM-CFRP. The free length can then be filled with mortar after cooling. Several investigations have been conducted on the feasibility and short-term behavior of RC elements strengthened with FeSMA, including experimental bond behavior [17–21], lab-scale beam tests [10,22–26], numerical (based on non-linear finite element analysis) studies [27–33], and real-world applications [34,35]. Other noteworthy applications include the use of Fe-SMA for shear strengthening of RC beams [36], strengthening of masonry walls [37] and self-centering columns [20,38].

The behavior of RC beams flexurally strengthened by Fe-SMA under long-term influences has not been investigated as thoroughly yet. Fe-SMA ribbed bars were investigated for their tension, possible recovery stresses, as well as stress relaxation. Stress relaxation losses in the range of 10% after 1000 h were observed [39]. An investigation of RC beams strengthened with unribbed NSM Fe-SMA bars after exposure to 650 freeze-thaw cycles and sustained load [40] reported that at the end of exposure the grout fixing the Fe-SMA was completely spalled, basically converting the NSM bar into an externally unbonded post-tensioned bar. Minimal signs of surface corrosion was noticed on the Fe-SMA bar, while the steel reinforcements had corroded significantly more. After repairing the spalled grout and subsequent bending loading until failure it was reported that freeze-thaw exposure resulted only in a minimal deterioration on the strengthened beam when compared to the unexposed beams.

Lastly, an interim reporting of the specimens investigated within this study was made after a four year exposure and sustained loading [41]. Comparison of the mid-span deflection from both beams displayed similar trends, attributed to the creep in the concrete and the effect of concrete flexural cracks. It was concluded that the reduction in prestressing force was not significant and stable.

The current study extends the results reported in [41] and compares the behavior observed within short-term experiments of [10] against an 8 year period of natural environmental exposure and sustained loading above the cracking load, followed by four-point loading. Most important details of [10] are also provided within this article to provide the reader the necessary information. To assess the applicability of existing analytical tools for both future behavior prediction and failure prognosis, a cross-section analysis based on [42] is employed, incorporating long-term material models specified in widely accepted guidelines. Moreover, a parameter study and subsequent sensitivity analysis, utilizing Sobol’ Indices [43], are implemented to investigate the effects of various parameters on the structural response.

**2. Experimental investigations**

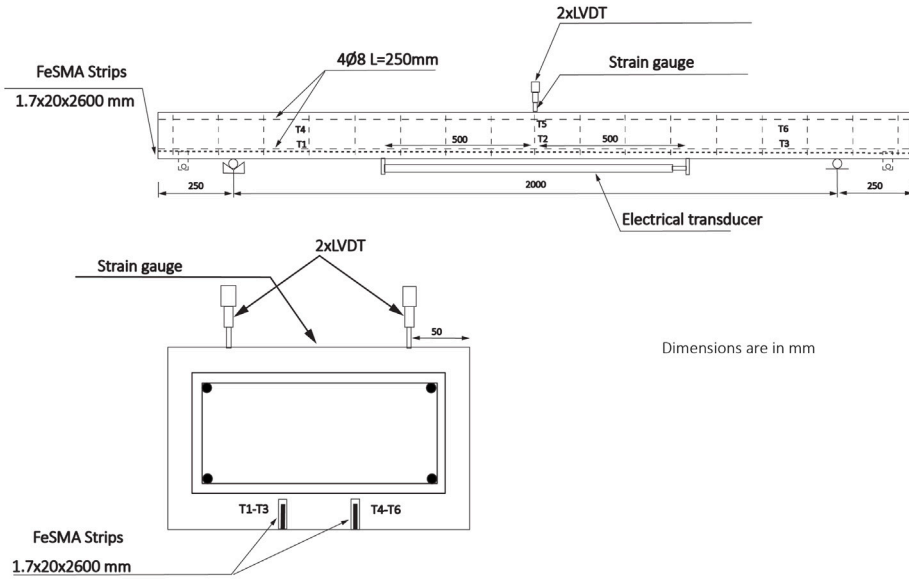
Experimental work and natural environmental exposure was conducted at the Swiss Federal Laboratories for Materials Science and Technology (Empa), on two additional two-meter span beams that were cast together with the other six beams previously presented in [10]. Both beams were placed outside and subjected under a four-point sustained loading setup for a duration of roughly 8 years. An overview of the experimental program, including the previous study is presented in Table 1. The following sections provide further detail pertaining to the used materials, measurement setup, and experimental procedure.

**2.1. Materials**

**2.1.1. Iron-based shape memory alloys (Fe-SMA)**

The FE–17Mn5Si–10Cr–4Ni–1(V, C) alloy, developed at the Swiss Federal Laboratories for Materials Science and Technology (Empa) in

### Phase 1, Activation Beam No:7



### Phase 2, Loading Beams No:7&8

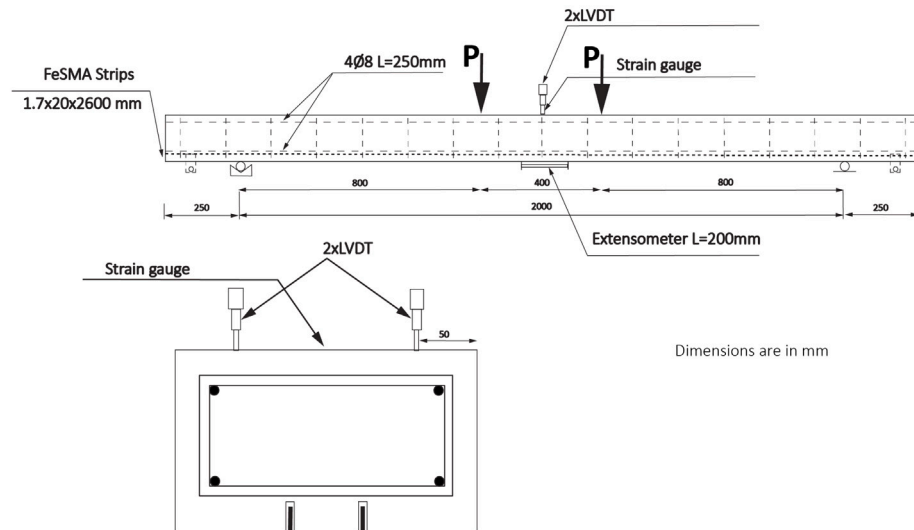


Fig. 2. Side view and cross-section of the beams during activation and loading.  
Source: Adopted from [10].

Switzerland, was previously presented in other studies, detailing the comprehensive production process and material assessment [44]. The final strip dimensions were 2.6 m in length, 20 mm in width, and with a nominal thickness of 1.7 mm, as shown in Fig. 1.

#### 2.1.2. Concrete, steel reinforcement, and grout

The beams were cast using a concrete mix comprising Type I Portland cement (350 kg/m<sup>3</sup>), coarse aggregate (maximum size: 16 mm), and a water–cement ratio of 0.50 by weight. For each beam, specimens

sized 150 × 150 × 150 mm were also cast and tested at 28 days and on the day of the experiment (for the short-term investigations presented in [10]). The compressive strength, splitting tensile strength, and elastic modulus of the concrete were measured after 28 days and determined to be 53.4 MPa, 3.4 MPa, and 35.4 GPa, respectively.

The internal reinforcement consists of four Ø8 mm longitudinal bars and Ø8 mm stirrups with a spacing of 150 mm, as shown in Fig. 2. The internal reinforcement exhibited an elastic modulus and yielding strength of 200 GPa and 508 MPa, respectively. The Fe-SMA

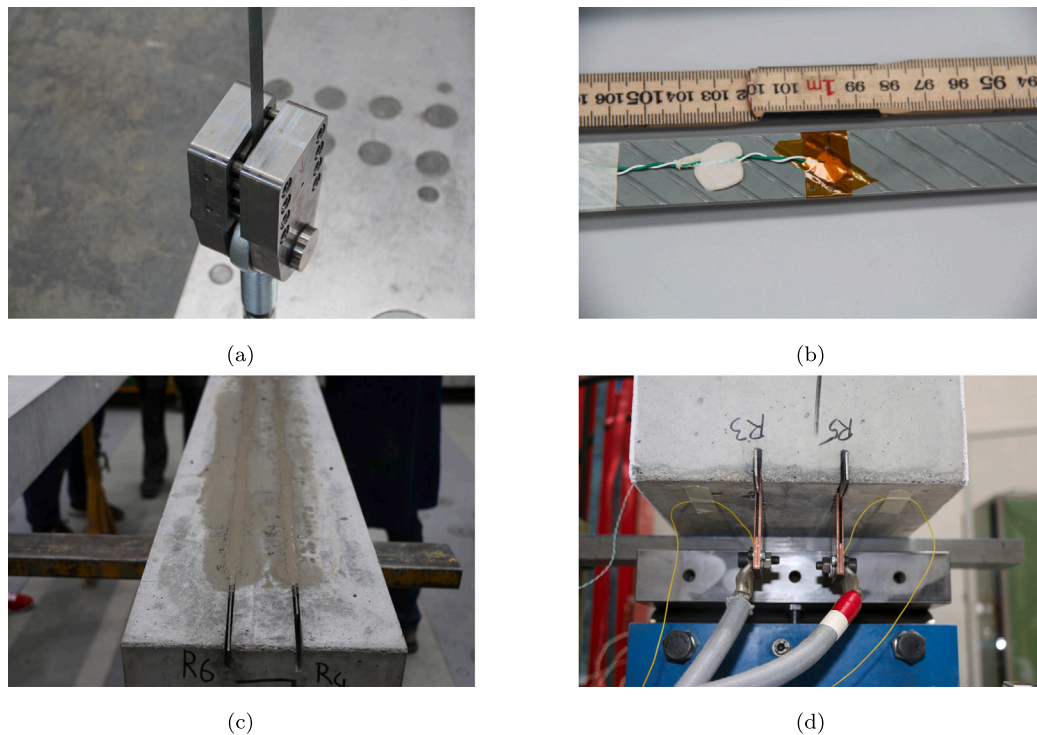


Fig. 3. (a) Clamps used for pre-straining the Fe-SMA strips, (b) Thermocouple installed on the strip, (c) Finished beam surface after installation of strips and grouting, (d) Copper clamps for resistive heating to activate the strips.

strips were bonded into the grooves via the commercially accessible flowable and expansive cement-based grout (SikaGrout-311). The manufacturer's technical datasheet specified that the mortar possessed an approximate maximum grain diameter size of 1.2 mm, compression strength of 80–90 MPa after 28 days, and an elastic modulus of 37.2 GPa.

## 2.2. Experimental procedure

The experimental procedure includes prestraining the strips, grouting of Fe-SMA strips in the grooves, activating the embedded strips within beams, subjecting the beams to sustained loading and environmental exposure for 8 years outdoors, and finally, transporting the beams back to the laboratory for loading until failure. The prestraining, activation and loading was performed in the year 2015. The unloading and loading to failure was performed in the year 2023. A detailed description of the procedure can be found in [10], but for the sake of completeness, a brief overview is provided herein.

### 2.2.1. Prestraining, grouting, activation

The Fe-SMA strips underwent pre-straining to 2% elongation at room temperature, using a manually operated oil hydraulic jack. Following this, the strips were allowed to relax to a stress-free state. To fix the Fe-SMA strips at their ends, steel clamps were employed, vertically fixed within an experimental setup on the strong floor (Fig. 3(a)).

Using a saw cut table machine, grooves measuring  $25 \times 6$  mm were created at the bottom of the beams. Prior to embedding the Fe-SMA strips into the concrete, three Type K thermocouples were attached to each strip. These thermocouples were positioned on the surface of the strips inside the concrete beams to monitor temperature changes (Fig. 3(b)). The SMAs were then placed inside the grooves and a cement-based grout was used to fill them, following the supplier's guidelines (Fig. 3(c)). Any remaining grout was removed, and the surface was smoothed.

Once the grout was fully cured, resistive heating was used to activate the strips of Beam 7 in series, whereas the strips of Beam 8 were left non-activated. The resistive heating was provided by a programmable electrical power supply and copper clamps, which was controlled by measured temperature of the strips inside the concrete beams (Fig. 3(d)). To minimize heating times and reduce heat flow into the concrete, a high current density of approximately  $9 \text{ A/mm}^2$  was applied. The activation process began when the temperature measured by selected thermocouples reached the target temperature of  $160^\circ\text{C}$ , at which point the power supply was switched off. Throughout the activation and subsequent cooling phases, mid-span displacements were monitored using two LVDTs. Additionally, strain measurements were recorded on both the top and bottom sides of the beam using strain gauges, with an additional 1-meter-long LVDT positioned on the bottom side of the concrete beams.

### 2.2.2. Long-term exposure

The two beams, one with activated Fe-SMA strips (Beam 7) and the other without (Beam 8), were supported simply at their ends and loaded using a concrete block weighing 1535 kg. The block was suspended at two loading points in the middle of Fig. 4(a) with a spacing of 400 mm. Long-term testing of both beams initiated on May 7th, 2015, outside the Structural Engineering Research Laboratory of Empa in Switzerland.

Since May 2015, mid-span deflection and crack propagation was monitored on both the activated and non-activated beams. The mid-span deflections were measured using a dial-gage LVDT (Fig. 4(b)), accompanied by temperature readings. Strain measurements on the upper and lower sides of the concrete were captured through mechanical strain gage measurements.

### 2.2.3. Four-point bending loading

The two long-term beams were subjected to four-point bending using two concentrated loads spaced 400 mm apart via two 50 kN hydraulic jacks (Fig. 5). The quasi-static loading was controlled by the left cylinder's displacement with a rate of  $0.02 \text{ mm/s}$ . First, five

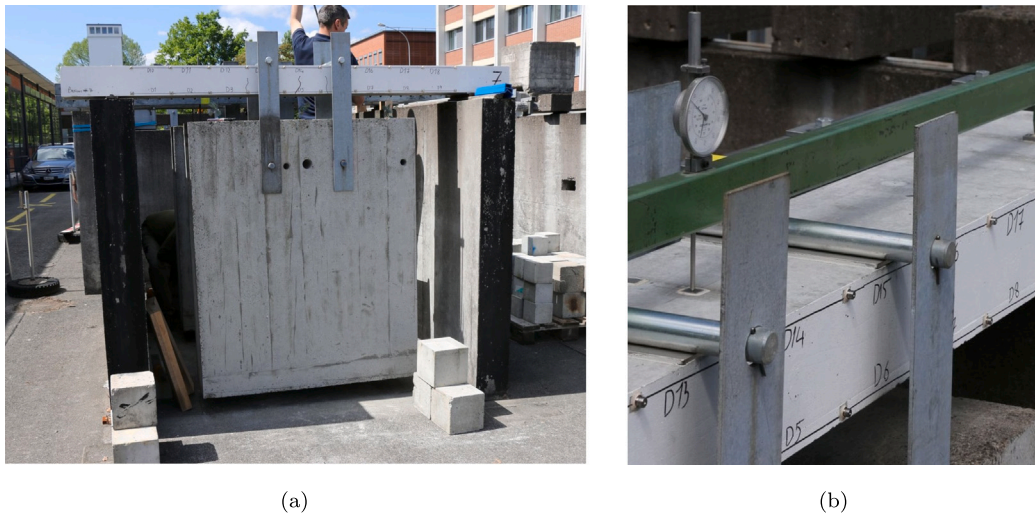


Fig. 4. (a) Sustained-loading setup outside the laboratory, (b) Dial-gage for the mid-span deflection and the pins used for the mechanical strain gage measurements.

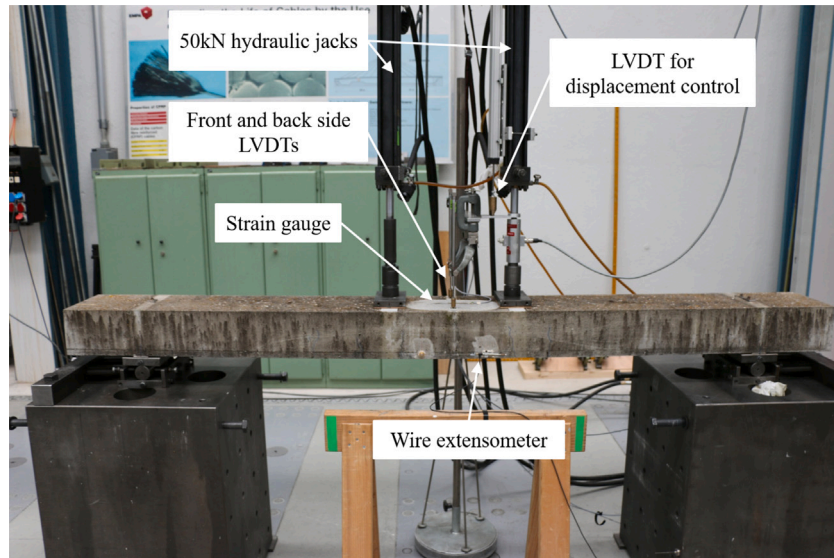


Fig. 5. Four-point bending experimental setup for testing the 8 year natural environmental exposed beams.

loading cycles between zero and a mid-span deflection of 1/500 of the span (i.e., 4 mm) was applied, even though the residual deflections following sustained loading were already higher than this value. This step was conducted to compare the loading-unloading slopes with the ones obtained in [10]. Upon completion of the fifth loading cycle, a monotonically increasing load was applied until failure. Mid-span deflections were measured by two LVDT's and the compressive concrete strain by a 10 cm long strain gauge. In contrast to the previous study, digital image correlation was not employed, but the strain in the Fe-SMA was still indirectly measured using an extensometer fixed 15 mm from the beam's bottom surface.

After failure, one beam was used as a host to obtain concrete drilling cores to investigate the aged concrete for its compressive strength. For this purpose, the location of stirrups were determined by a magnetic induction scanner (Ferroscan PS200, Hilti) and 7 cores with a diameter of  $\varnothing 75$  mm were collected from Beam 7 and tested for its compressive strength according to SN EN 13791:2019 [45] and the carbonation depth measured. Additionally, the concrete at bottom face of the beam within the constant moment region was removed to see if any corrosion took place during the 8 year exposure.

### 3. Numerical investigations

#### 3.1. Long-term effects

The formulation of long-term effects discussed in the following section is largely adopted from the fib Model Code 2020 [46]. In order to provide a comprehensive introduction to the numerical investigations, a brief summary is included in the following sections. For further details and a more comprehensive examination, interested readers are encouraged to refer to the original cited document.

##### 3.1.1. Development of material properties with time

The development of concrete compressive strength with time is estimated with Eq. (1).

$$f_{cm}(t) = \beta_{cc}(t) \cdot f_{cm}, \text{ with } \beta_{cc} = \exp \left\{ s \cdot \left[ 1 - \left( \frac{28}{t} \right)^{0.5} \right] \right\} \quad (1)$$

The coefficient  $s$  depends on the strength class of cement and can take the values of 0.38, 0.25 and 0.20.

The development of concrete Young's modulus with time is estimated with Eq. (2).

$$E_{ci}(t) = \beta_E(t) E_{ci}, \text{ with } \beta_E(t) = [\beta_{cc}(t)]^{0.5} \quad (2)$$

The initial compressive strength  $f_{cm}$  and Young's modulus  $E_{ci}$  are the values measured at 28 days.

### 3.1.2. Creep and shrinkage

Total strain of concrete at time  $t$  consists of the following sum:

$$\varepsilon_c(t) = \varepsilon_{ci}(t_0) + \varepsilon_{cc}(t) + \varepsilon_{cs}(t) + \varepsilon_{cT}(t) \quad (3)$$

where  $\varepsilon_{ci}(t_0)$  is the initial strain at loading,  $\varepsilon_{cc}(t)$  is the creep strain at time  $t \geq t_0$ ,  $\varepsilon_{cs}(t)$  is the shrinkage strain at time  $t$  and  $\varepsilon_{cT}(t)$  is the thermal strain at time  $t$ . Out of these components,  $\varepsilon_{ci}(t_0)$  and  $\varepsilon_{cc}(t)$  are defined as stress dependent strains, whereas the others are defined as stress independent strains.

The stress dependent strains  $\varepsilon_{cc}$  are formulated as in Eq. (4)

$$\varepsilon_{cc}(t, t_0) = \sigma_c(t_0) \cdot J(t, t_0) = \sigma_c(t_0) \cdot \left[ \frac{1}{E_{ci}(t_0)} + \frac{\varphi(t, t_0)}{E_{ci}} \right] \quad (4)$$

where  $J(t, t_0)$  is the creep compliance function, representing the total stress dependant strain per unit stress. The term  $\varphi(t, t_0)$  within the compliance function represents the creep coefficient and can be calculated as:

$$\varphi(t, t_0) = \varphi_0 \cdot \beta_c(t, t_0) \quad (5)$$

where  $\varphi_0$  is the notional creep coefficient and is defined as

$$\varphi_0 = \varphi_{RH} \cdot \beta(f_{cm}) \cdot \beta(t_0) \quad (6)$$

with

$$\varphi_{RH} = \left[ 1 + \frac{1 - RH/100}{0.1 \sqrt[3]{h}} \cdot [35/f_{cm}]^{0.7} \right] \cdot [35/f_{cm}]^{0.2} \quad (7)$$

$$\beta(f_{cm}) = \frac{16.8}{f_{cm}} \quad (8)$$

$$\beta(t_0) = \frac{1}{0.1 + (t_0)^{0.2}} \quad (9)$$

The input variables  $RH$  and  $h$  represent the relative humidity of the ambient environment and notional size of the member, respectively.

Neglecting the thermal effects, the stress independent strains reduce to only shrinkage induced strains, which is formulated as in Eq. (10).

$$\varepsilon_{cs}(t, t_s) = \varepsilon_{cas}(t) + \varepsilon_{cds}(t, t_s) \quad (10)$$

where  $\varepsilon_{cas}(t)$  and  $\varepsilon_{cds}(t, t_s)$  denoting the autonomous and drying shrinkage strains, respectively. The autonomous shrinkage strain is calculated by:

$$\varepsilon_{cas}(t) = \varepsilon_{cas0}(f_{cm}) \cdot \beta_{as}(t) \quad (11)$$

with

$$\varepsilon_{cas0}(f_{cm}) = -\alpha_{as} \left( \frac{f_{cm}/10}{6 + f_{cm}/10} \right)^{2.5} \cdot 10^{-6} \quad (12)$$

$$\beta_{as}(t) = 1 - \exp(-0.2\sqrt{t}). \quad (13)$$

The drying shrinkage strain is calculated by:

$$\varepsilon_{cds}(t, t_s) = \varepsilon_{cds0}(f_{cm}) \cdot \beta_{RH}(RH) \cdot \beta_{ds}(t - t_s) \quad (14)$$

where

$$\varepsilon_{cds0}(f_{cm}) = [(220 + 110 \cdot \alpha_{ds1}) \cdot \exp(-\alpha_{ds2} \cdot f_{cm})] \cdot 10^{-6}, \quad (15)$$

$$\beta_{ds}(t - t_s) = \left( \frac{(t - t_s)}{0.035h^2 + (t - t_s)} \right)^{0.5}, \quad (16)$$

$$\beta_{s1} = \left( \frac{35}{f_{cm}} \right)^{0.1} \leq 1.0, \quad (17)$$

$$\beta_{cds0} = \begin{cases} -1.55 \left[ 1 - \left( \frac{RH}{100} \right)^3 \right], & \text{for } 40 \leq RH \leq 99\% \cdot \beta_{s1}. \\ 0.25, & \text{for } RH \geq 99\% \cdot \beta_{s1}. \end{cases} \quad (18)$$

The coefficients  $\alpha_{as}$ ,  $\alpha_{ds1}$  and  $\alpha_{ds2}$  are dependent on the strength class of the cement.

### 3.2. Cross-section analysis

The cross-sectional analysis employed within the presented study is an extension of a previous work by the first author [42] incorporating long-term effects into the calculation, and the basics are briefly summarized herein. Even though it was originally conceptualized for RC beams strengthened with prestressed unbonded CFRP strips, it has since then customized and generalized and employed for prestressed bonded CFRP strips [47,48] and for FRCM [49].

It relies on establishing force equilibrium between compressive and tensile forces, as expressed in Eq. (19), for a given curvature  $\kappa$  (see Fig. 6).

$$\Delta F = F_c + F_{s'} + F_s + F_{SMA} = 0 \quad (19)$$

The strains within the cross-section can be expressed as a function of the two variables concrete top-fiber strain ( $\varepsilon_c$ ) and neutral axis depth ( $x_c$ ). For an efficient computation, a vectorized approach can be adopted. Consequently, the cross-sectional strains can be represented as a matrix that contains all possible combinations of  $\varepsilon_c$  and  $x_c$ , as exemplified in Eq. (20) for the tensile steel reinforcement, where the symbol  $\odot$  denotes the Hadamard product and  $\otimes$  denotes the Kronecker product. If  $\vec{\varepsilon}_c$  is an  $n \times 1$  and  $\vec{x}_c$  is an  $m \times 1$  vector, the cross-sectional strains take the form of an  $n \times m$  matrix.

$$\underline{\underline{\varepsilon_s}} = \left[ (d - \vec{x}_c) \odot \frac{1}{\vec{x}_c} \right] \otimes \vec{\varepsilon}_c^T \quad (20)$$

Once all the strain matrices are calculated, the internal forces necessary for force equilibrium can be derived. Matrix-based formulation of the concrete compressive forces  $F_c$  is given in Eq. (21).

$$\underline{\underline{F_c}} = f_{c,cyl} \cdot b \cdot (\vec{x}_c \otimes \vec{\alpha}_c) \quad (21)$$

, where  $f_{c,cyl}$  is the cylinder compressive strength of concrete,  $b$  the width of the beam and  $\vec{\alpha}_c$  is the  $\vec{\varepsilon}_c$  based concrete stress block coefficients [50]. The forces in the steel reinforcement are also formulated in a vectorial format, relying on an elastoplastic law with linear hardening.

The forces in the NSM Fe-SMA is calculated using the stresses obtained from tensile testing. The forces from each component are summed up to calculate the  $\Delta F$  matrix, where each element of this matrix represents the force resultant in the section due to a specific combination of  $\varepsilon_c$  and  $x_c$ . For every value of  $\varepsilon_c$ , there exists a corresponding  $x_c$  value that satisfies equilibrium ( $\Delta F \approx 0$ ).

Subsequently, the internal moments are calculated and the total moment vs. curvature relationship is derived. As a next step, an external moment distribution along the beam can be provided at discretized locations to extract the curvatures and analogously strains along the beam. Finally, the midspan deflection  $\delta$  can be determined by double integrating the curvature distribution over the span.

## 4. Results and discussion

### 4.1. Prestraining

The stress-strain behavior of the Fe-SMA used in beams 7 and 8 can be observed in Fig. 7. The applied prestrain reached a level of 2%, and upon unloading, a residual strain of about 1.5% remained. Prior to prestraining, the strips were in the austenite phase, and the observed nonlinear deformation can be attributed to a partial phase transformation from austenite to martensite. The nonlinearity observed during unloading can be ascribed to the elastic and pseudoelastic strain, indicating a partial phase transformation back to austenite [44].

The expected recovery stress, based on previous experimental observations in [10] lie in the range of 220–250 MPa, when heated to a maximum temperature of 160 °C.

Specimens extracted from initial full-width strips were tested until failure, the stress-strain plot is provided in Fig. 8. It can be observed

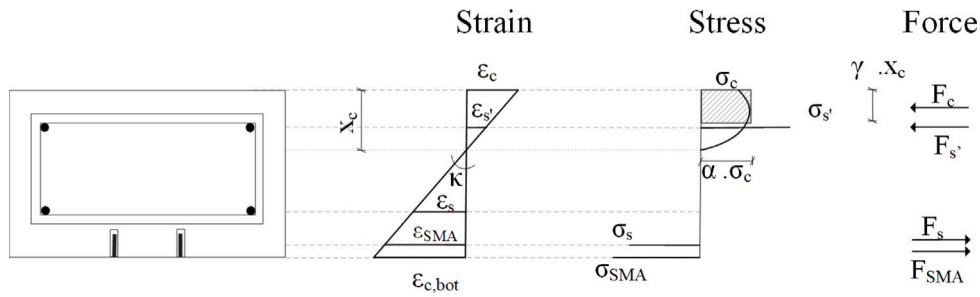


Fig. 6. Beam cross-section and strain, stress and force distribution under an arbitrary loading stage.

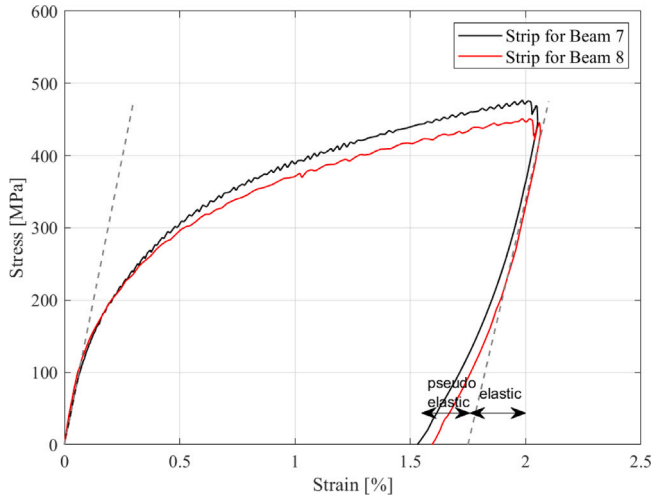


Fig. 7. Stress-strain behavior during loading and unloading steps of pretraining. Gray dashed lines are provided to visualize the non-linear divergence due to partial phase transformations.

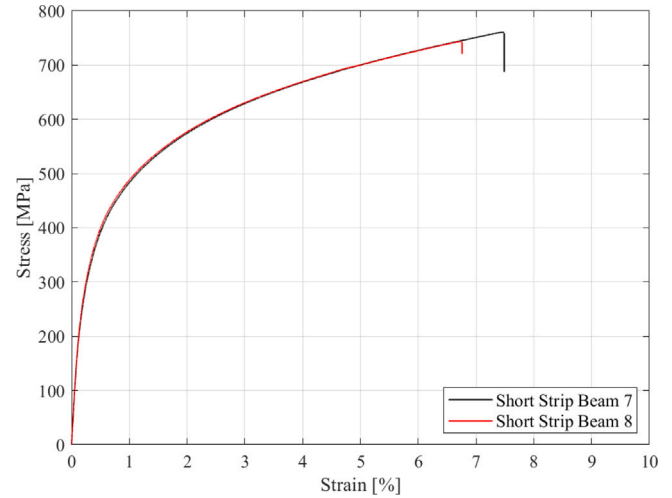


Fig. 8. Stress-strain relationship of SMA specimens obtained from initial full-width strips, monotonic tensile testing.

that tensile failure occurs above 700 MPa of stress and a strain well above 5%. It shall be noted that current versions of FeSMA possess an ultimate strain beyond 40% [44], the lower ultimate strain of the alloy employed herein is due to it being from one of the first batches of FeSMA production.

#### 4.2. Activation of Fe-SMA strips in beam #7

The applied voltage, power, energy on the SMA strips, the recorded temperatures of the thermocouples and mid-span deflection during resistive heating activation of Beam 7 are presented in Fig. 9.

It can be seen that the temperature rapidly increases within the 12 s heating period, followed by a gradual cooling while the shape memory effect is already taking place. A significant variation was observed among the thermocouples, which aligns with similar observations made in [10]. This high variation can be attributed to the fact that the thermocouples were not in direct contact with the strips due to electrical current flowing through them during activation. Consequently, they were installed with electrical isolation, resulting in an uncertain and potentially varying distance between the thermocouples and the strips at different installation locations. This variation, on the other hand, indirectly indicates a high thermal gradient between the SMA strips and the surrounding concrete, suggesting that concrete does not reach the same elevated temperatures as the activation temperature.

As visible from Fig. 9, the beam deflects during the first 1.7 s (48 °C at thermocouple T4) downwards due to the thermal expansion of SMA strips, until the onset of the shape memory effect. Then, the shape memory effect causes the beam to deflect upwards, as expected. The mid-span deflection appears to be stable at −0.15 mm within the first 24 h of activation, as shown in Fig. 10.

#### 4.3. Long-term sustained loading and natural environmental exposure

Since the application of sustained load on May 7th, 2015, a clear deformation trend has been observed in both beams. Fig. 11 indicates an immediate deformation after loading, followed by an increase at a decreasing rate. As anticipated, Beam 7 with activated SMA strips demonstrates lower initial and long-term deflections. Both beams experience their main deformations within the first three months. The instantaneous mid-span deflections measure 4.3 mm and 7.3 mm for beams 7 and 8, respectively. Just before unloading on March 16th, 2023, these values had increased to 10.3 mm and 13.6 mm, respectively. Subsequently, on the same day, instantaneous reversible deflections were measured at approximately 1.8 mm and 2.4 mm for beams 7 and 8, respectively.

A further exploration of the long-term response of both beams can be made via the strains at mid-span, which were measured using a mechanical strain gage, as shown in Fig. 12. The instantaneous strains at a distance of 10 mm from the top and bottom faces reached −0.09% and 1.68% for Beam 7 and −0.11% and 3.66% for Beam 8, respectively. The strains reached values of −0.58% (last measured value on 09/12/2021 before the measurement pin detached) and 2.54% for Beam 7 and for −0.61% and 5.43% Beam 8, just before unloading. After unloading, the strains were measured at −0.36% and 2.14% for Beam 7 and −0.40% and 4.32% for Beam 8. Once again, the effect of prestressing by SMA activation is evident from the reduced strains measured on the bottom side of the beams. However, on the top side, this difference is less pronounced, as the top strain evolution relies more heavily on the creeping of concrete.

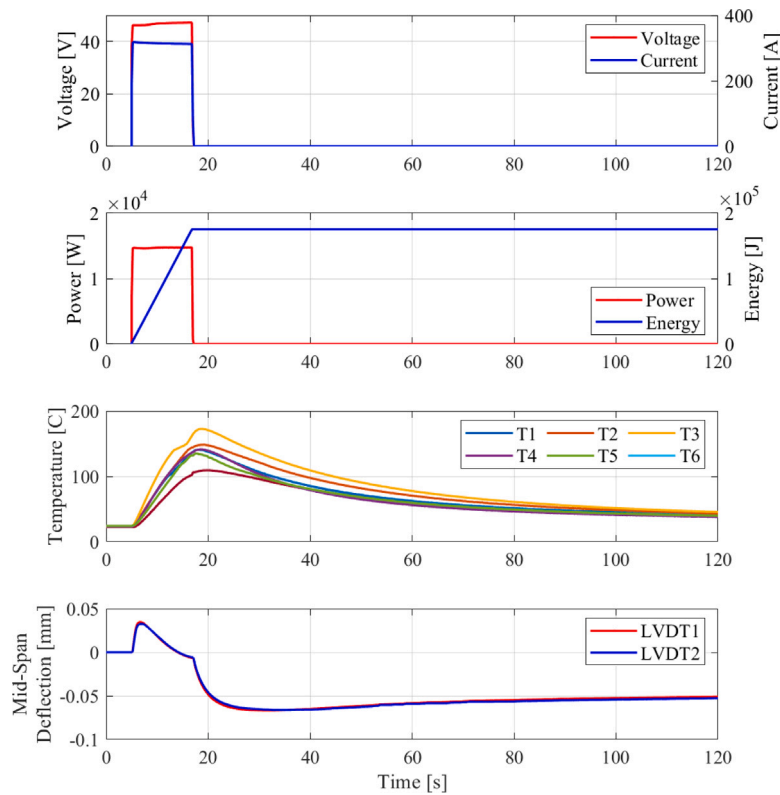


Fig. 9. (i) Applied voltage/current and (ii) power/energy, (iii) measured temperatures and (iv) mid-span deflections (– upward, + downward) during the first two minutes of activation via resistive heating of Beam 7.

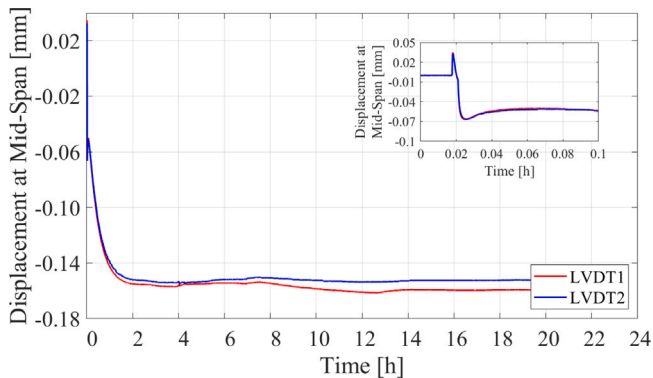


Fig. 10. Mid-span deflection behavior of Beam 7 within the first 24 h of activation. Negative values represent an upward lift of the beam.

#### 4.4. Structural behavior of tested beams and post-failure investigations

The response of the two beams subjected to 4-point bending load, as shown in Fig. 13, was compared to beams from [10], Table 2 in order to investigate the impact of 8 years of natural environmental exposure and sustained loading on bending behavior. It is a general that additional reinforcement increases the yielding and ultimate strength of RC beams and that prestressing enhances the cracking and yield strength, while not affecting the ultimate load but decreasing ultimate deflection at failure [5]. Expanding upon this definition by introducing the new specimens, it can be observed that the bending behavior does not undergo significant changes following long-term exposure and sustained loading. No signs of deterioration was observed within the structural response of both beams, if the residual displacements after sustained loading are also considered. Furthermore, as can be

seen in Fig. 13(b), the cracked stiffness during load cycling did not reveal any noticeable degradation in slope when compared to identical beams from [10]. The starting point in Fig. 13 for both exposed beams was determined from the measured residual mid-span deflections after unloading (see Fig. 11).

The average ultimate load was 16.8 kN and  $16.7 \pm 0.26$  kN, for unexposed beams from [10] with non-activated and activated SMA strips, respectively. Average mid-span deflection of these beams were recorded to be 70.6 mm and  $53.3 \pm 3.12$  mm. In comparison, Beam 8 with non-activated SMA strips had an ultimate load of 16.4 kN and a mid-span deflection of 67.9 mm, while Beam 7 with activated SMA strips had an ultimate load of 17.1 kN and a mid-span deflection of 56.2 mm.

To further investigate the bending behavior of both beams following sustained loading and natural environmental exposure, a comparison of their top concrete and SMA strains are made. In this study, the top concrete strains were measured in a manner identical to [10]. However, the SMA strains were measured using LVDTs on the lower side of the beam, as opposed to the DIC measurements. The measurement location and distance of DIC measurements were replicated with the LVDTs to ensure a reasonable comparison. The results for SMA strains are presented in Fig. 14(a), while concrete strains are shown in Fig. 14(b). The initial strain values for Beam 7 and Beam 8 during their four-point bending loading were derived from the long-term deformer measurements, as previously provided in Fig. 12.

Similar to the force vs. mid-span deflection behavior, both SMA and concrete strains eventually align with the beams that did not undergo sustained loading and natural environmental exposure. SMA strains at concrete crushing correspond to 2% and 3.57% for Beams 7 and 8, respectively. Maximum top concrete strains were recorded at  $-3.06\%$  and  $-3.38\%$  for Beams 7 and 8. A slight increase in post-yielding stiffness can be observed for both beams and at both measured strain locations. This increase is likely attributed to the enhanced strength

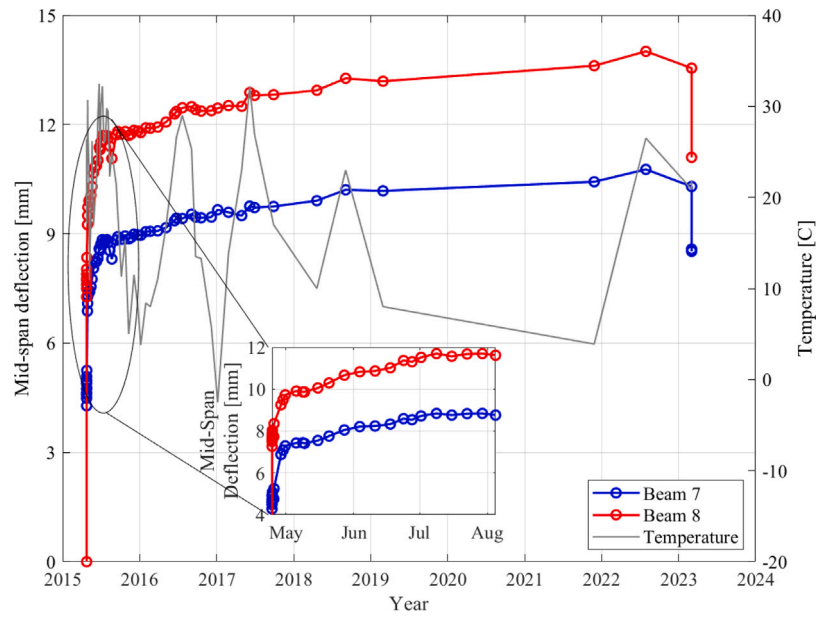


Fig. 11. Recorded mid-span deflections of both beams during natural environmental exposure and sustained loading.

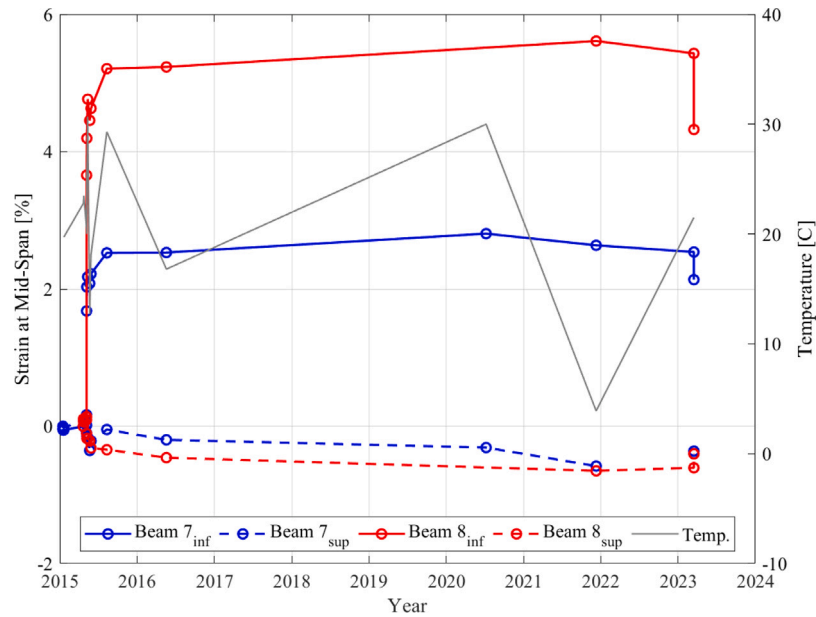


Fig. 12. Recorded top- and bottom strains (– compression, + tension) of both beams during natural environmental exposure and sustained loading.

Table 2

Overview of experimental results (Beams 1 to 6 are taken from Shahverdi et al. [10]).

Beam No.	Failure mode	$F_{max}$ [kN]	$\delta_u$ at $F_{max}$ [mm]
1	Concrete crushing after steel yielding	9.8	48.7
2	Concrete crushing after steel and SMA yielding	16.8	70.6
3, 4, 6	Concrete crushing after steel and SMA yielding	$16.7 \pm 0.26$	$53.3 \pm 3.12$
7	Concrete crushing after steel and SMA yielding	17.1	56.2
8	Concrete crushing after steel and SMA yielding	16.4	67.9

and stiffness of the concrete, which is further numerically analyzed and discussed in the subsequent section.

At the end of sustained loading and natural environmental exposure, as well as after the four-point bending tests, the cracking patterns were examined and mapped. During the four-point bending tests, only a limited number of new cracks were observed, while the majority of cracking was attributed to the propagation of existing cracks. This is

evident from the cracking patterns depicted in Fig. 15. As expected, Beam 8 with non-activated SMA strips experienced a more densely spaced cracking, compared to Beam 7 with activated SMA strips.

Another future step that was taken was to take one of the beams (Beam 7) and extract further information from the already examined specimens. To this end, the beam was scanned in all directions with a magnetic induction scanner (Ferrosan PS200, Hilti) and the

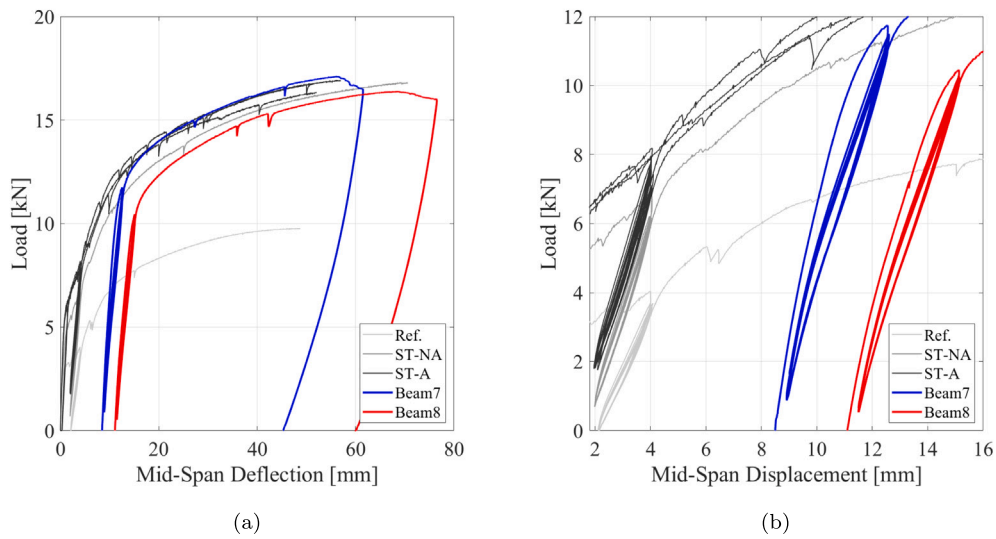


Fig. 13. Load vs. mid-span deflection of short-term beams from [10] together with the recently tested beams after 8 years up to failure (a) and within initial cycling (b).

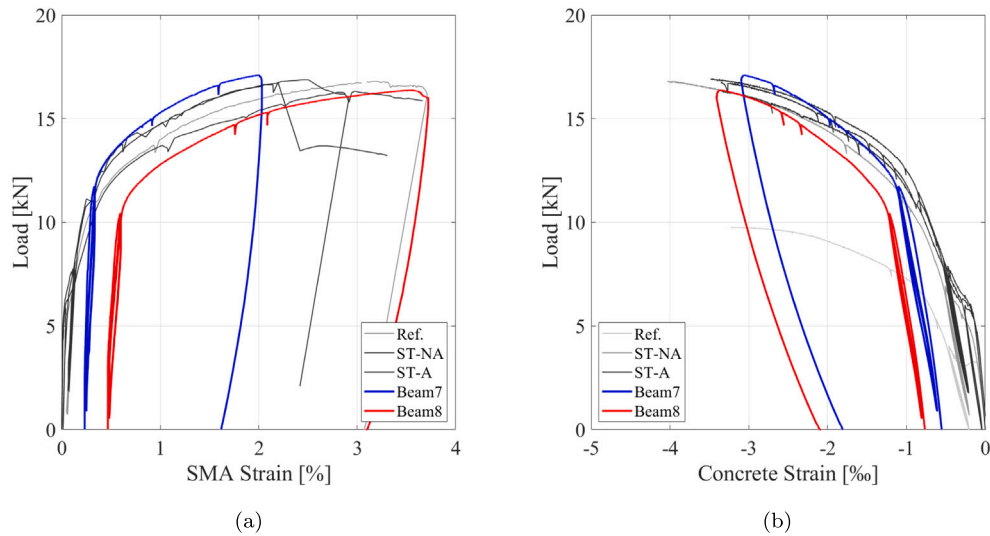


Fig. 14. Load vs. strain of short-term beams from CITE together with the recently tested beams for SMA (a) and for top concrete (b).

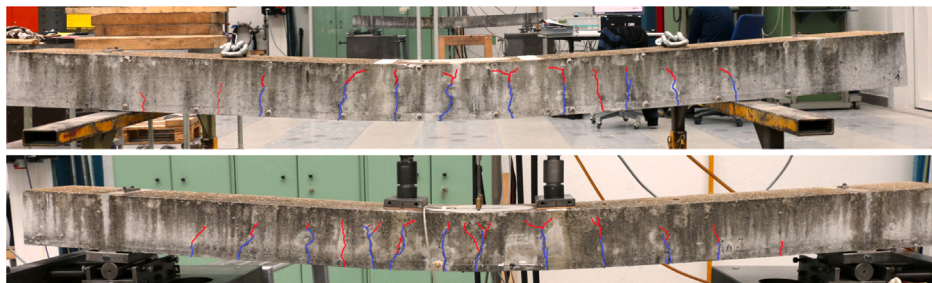


Fig. 15. Cracking patterns after sustained loading and natural environmental exposure (in blue) and subsequent four-point bending tests (red) for Beams 7 (top) and 8 (bottom). (For interpretation of the references to color in this figure legend, the reader is referred to the web version of this article.)

reinforcements located. Subsequently, seven concrete cores with  $\varnothing 75$  mm diameter were extracted from the uncracked regions of the beam in between the reinforcements (see Fig. 16(a)), three of which were subsequently tested for their compressive strength according to SN EN 13791:2019 [45] and the carbonation depth measured. The results of compressive tests are provided in the following section as part of the

numerical investigations. The carbonation depth of all tested concrete cores was between 4 to 8 mm.

Additionally, the concrete within the constant moment region of the underside of the beam was removed to see if any corrosion took place during the 8 year exposure. As seen in Fig. 16(b), no visible corrosion or cross-section reduction was observed, as expected based



Fig. 16. Four of the extracted concrete cores from Beam 7 (a) and exposed reinforcements at the bottom face within the constant moment region (b).

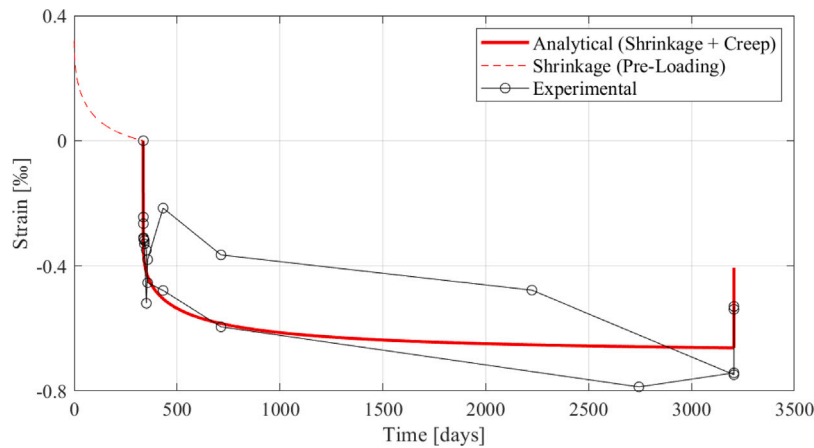


Fig. 17. Analytically calculated shrinkage and creep strains of the concrete compressive strain at beam mid-span versus recorded concrete strain during sustained loading and environmental exposure.

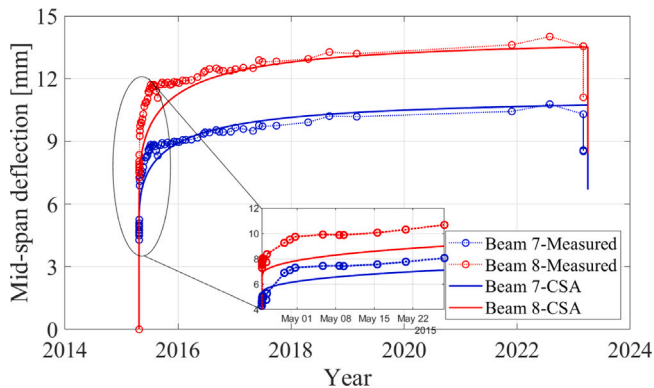


Fig. 18. Recorded and calculated mid-span deflections of both beams during natural environmental exposure and sustained loading.

on the carbonation depth not reaching the reinforcements yet. The SMA strips are marginally within the carbonated concrete cover, yet no signs of stress corrosion was observed. It is, however, recommended that the SMA strips are also applied within a clear cover depth specified by design guidelines to minimize the risk of corrosion.

#### 4.5. Cross-section analysis and parameter sensitivity

The cross-section analysis method described in Section 3 was employed in several ways throughout this section. First, the long-term

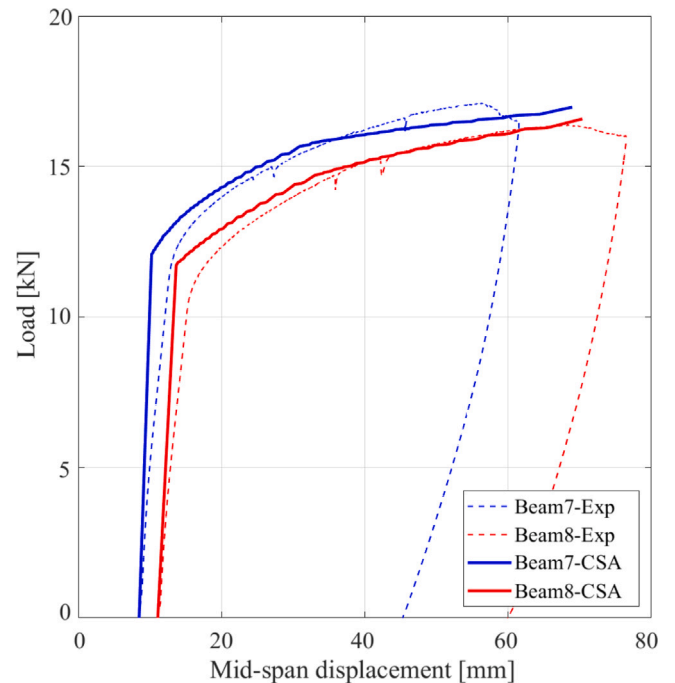


Fig. 19. Recorded and calculated load vs. mid-span deflection of beams after 8 years up to failure.

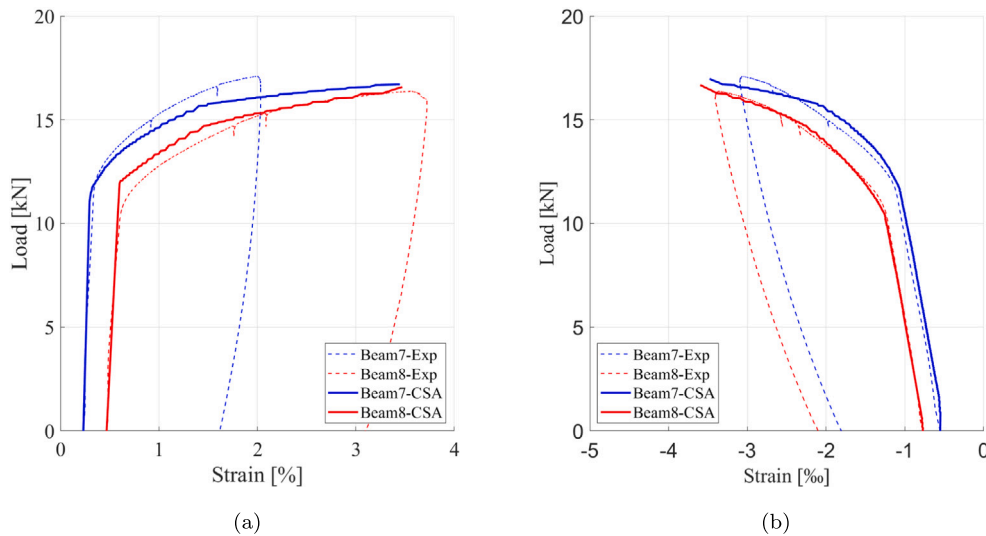


Fig. 20. Load vs. measured and calculated strain of beams for SMA (a) and for top concrete (b).

response of both beams during their natural environmental exposure under sustained loading was simulated, also considering time effects such as concrete creeping and SMA stress relaxation. Then, the 4-point bending loading response of both beams until failure were simulated to understand the validity of material models following long-term exposure. Finally, sensitivity analysis was conducted to further explore the effects of certain parameters on the long-term and monotonic loading response, utilizing the common one-at-a-time (OAT) approach as well as a multiple-output sensitivity via Sobol' indices [51].

#### 4.5.1. Long-term material and system behavior

For the long-term behavior calculations, the chosen concrete creeping and shrinkage models were validated, which are based on the fib Model Code [46]. To this end, the concrete compressive strains measured at mid-span of the beams were compared against these models. It is worth mentioning that shrinkage begins even before any external sustained loading is applied, yet these strains were not measured until the introduction of loading. Consequently, the initial and significant part of shrinkage was not experimentally captured and can only be estimated using the fib Model Code equations, as depicted in Fig. 17 with the red dashed line. In order to facilitate a proper comparison of the analytical equations with the measurements, the zero point was set to the day of sustained loading. The thick continuous red line, when compared to the experimental observations in the same figure, demonstrates that the continuing shrinkage and concrete creeping are reasonably approximated by the fib Model Code equations. This validation provides confidence in the accuracy of the chosen models for predicting the long-term behavior of the concrete.

After successfully validating the concrete creep and shrinkage models, the cross-section analysis script was enhanced to include the concrete compressive strength evolution and an assumed constant 10% SMA stress relaxation [44]. Subsequently, the structural response was simulated for the entire duration of sustained loading and natural environmental exposure for both beams with activated and non-activated SMA strips. Fig. 18 demonstrates that the long-term response, as represented by mid-span deflections, was reproduced accurately through the cross-section analysis. However, it was observed that the calculated reduction of the mid-span deflection after unloading was higher than the experimental observations. This deviation occurred despite the consideration of the time-dependent increase of the elastic modulus of concrete in the unloading portion of the compliance function. One possible explanation might lie in certain phenomenon that was not considered at this stage, such as tension stiffening, but was not further investigated.

Table 3

Calculated mid-span deflections immediately after loading (2015) and before unloading (2023), and their respective contribution to the total deflection, assuming a 10% stress relaxation in the activated SMA strip.

Contribution to $\delta_s$	Beam 7		Beam 8	
	$\delta$ [mm]	Contribution [%]	$\delta$ [mm]	Contribution [%]
Loading contribution	4.74	44.15%	6.00	44.40%
Creep contribution	5.48	51.11%	5.62	41.59%
Shrinkage contribution	0.51	4.74%	1.89	14.01%
Total	10.73	100.00%	13.51	100.00%

#### 4.5.2. Bending response during 4-point loading

The bending response was simulated by incorporating the most recent material values at the time of loading. The mean concrete compressive strength obtained from extracted concrete cores was 91.9 MPa. The size effect was considered by the equations recommended by Kim et al. [52]. A good agreement was observed between the size-effect compensated experimental value of 76.6 MPa and the fib Model Code prediction of 73.2 MPa. The 10% stress relaxation of SMA from Shahverdi et al. [44] was also incorporated into the CSA as a constant value for Beam 7. The response of both beams under monotonic four point bending loading are presented in Fig. 19 for their load vs. mid-span deflection behavior, in Fig. 20 for their load vs. SMA strain and concrete strain, respectively. It is important to mention that these figures exclusively represent CSA results beginning from the experimentally observed residual displacements. Calculation results preceding these displacements have been omitted to improve their readability.

It is evident from those figures that the bending response of both beams is accurately reproduced, effectively capturing the yielding and ultimate loads, as well as pre- and post- yielding stiffness and ultimate deflections. The post-yielding slope (of all reinforcements) of the CSA result of Beam 7 is flatter than the experimental observations, which might be linked to the constitutive model (experimental data) used for the SMA.

#### 4.5.3. Parametric study and sensitivity analysis

After demonstrating the accuracy of the CSA script, further computations were conducted to gain insights into the impact of different effects (loading dependent or time-dependent) on the final results and to assess the significance of each parameter in the overall structural behavior. This comprehensive investigation involved various approaches and tools to analyze both the long-term response and four-point bending behavior of the beams

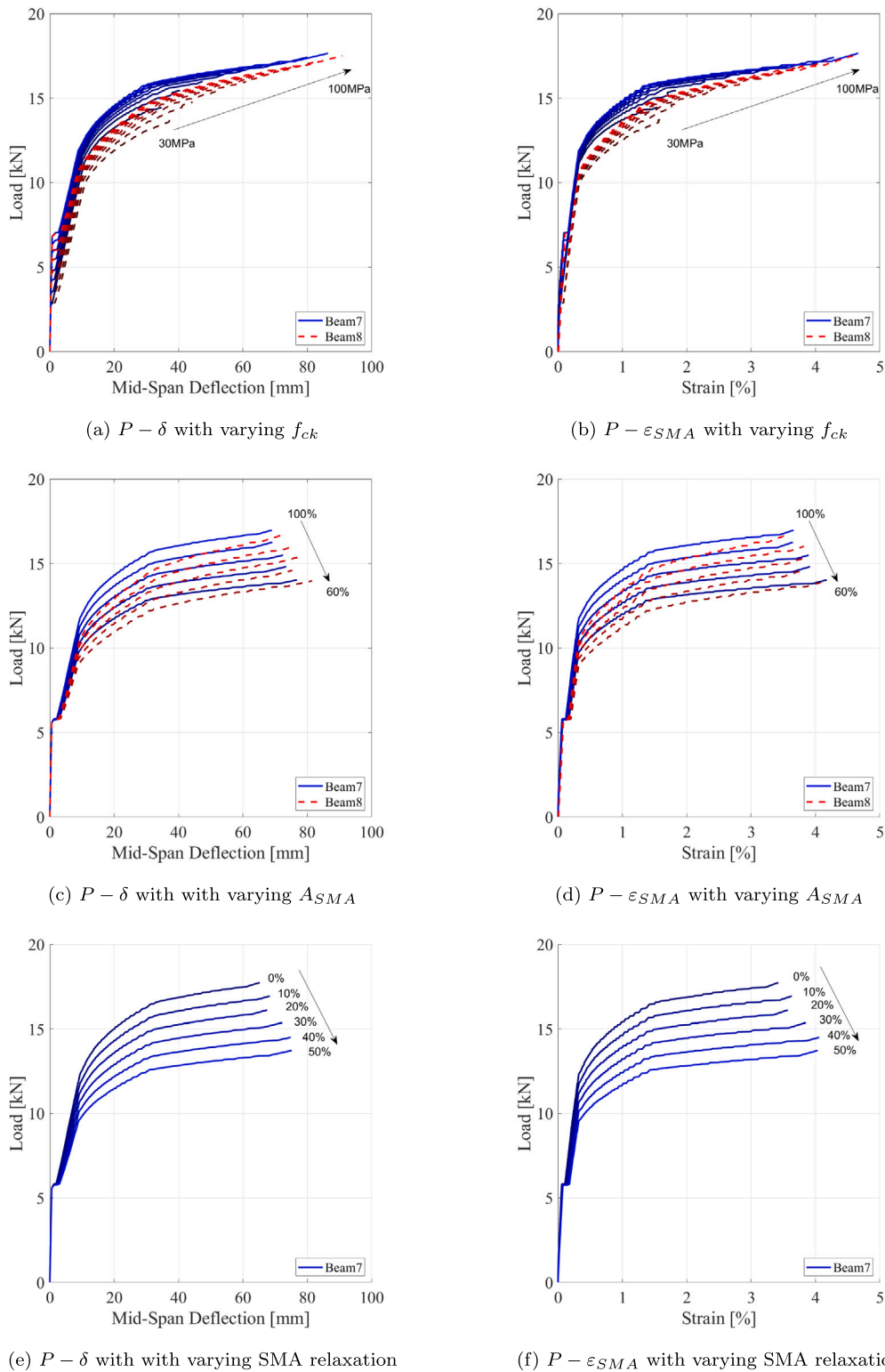


**Fig. 21.** Load vs. mid-span deflection (left column) and SMA strain (right column) response of both beams with differing  $f_{ck}$  (30–100 MPa, top row), SMA area (%60–%100, middle row) and SMA relaxation (%0–%50, bottom row).

At a first step, the CSA was used to examine the contribution of mechanical loading, load-dependent, and load-independent long-term effects (e.g., creep and shrinkage) to the total mid-span deflection, as shown in Table 3. At the moment of loading, the mid-span deflection is solely a result of mechanical effects. However, after the 8 year testing period, the contribution of mechanical loading reduces to 44% of the total mid-span deflection. The contribution of shrinkage was

determined by simulating the behavior without any sustained loading (only self-weight, which already exists at the time of loading and thus is not registered as an immediate deflection). Consequently, the contribution of concrete creep is what remains after subtracting the deflections caused by mechanical loading and concrete shrinkage. Since the stresses induced by sustained loading are considerably higher than the decompression caused by activating the SMA strips, the deflection

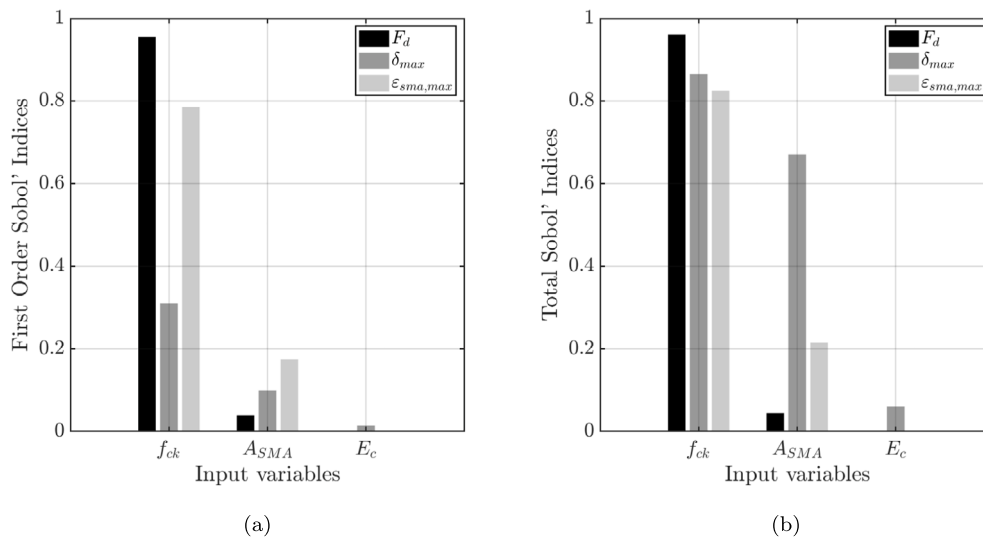


Fig. 22. (a) First Order and (b) Total Sobol' indices for ultimate force, mid-span deflection and SMA strain responses with concrete compressive strength, SMA cross-section area and concrete Young's modulus as input variables.

attributed to concrete creep is not significantly different between the two tested beams. Nonetheless, due to the lower total deflections for the activated beam, the contribution of creep to the total deflection appears higher for Beam 7.

As a next step, the four-point bending response was simulated for various values of the input parameters  $f_{ck}$ , SMA area and SMA relaxation via the conventional one-at-a-time parametric study approach and the results presented in Figs. 21. The compressive strength was varied between 30–100 MPa, the SMA area between 60%–100% of the experimental setup and the SMA relaxation between 0%–50%. The FeSMA relaxation values above 10% are purely hypothetical results and are only simulated for discussion purposes.

Increasing the concrete compressive strength from 30 MPa to 100 MPa causes a 14.2% and 27.5% increase in the ultimate load for the activated and non-activated beams, respectively. For both beams, the mid-span deflection and the SMA strain at concrete crushing more than doubles with such an increase in compressive strength. These observations suggest that the change in strength has a greater impact on the response of non-activated beams, as expected due to the absence of external prestressing forces.

Changing the SMA cross-sectional area from 60 to 100% of the experimental setup causes approximately a 20% increase in the ultimate load as well as yielding point, a 10% decrease in the mid-span deflection and SMA strain at concrete crushing, both for the activated and non-activated beams.

Varying the SMA stress relaxation beyond the realistically assumed 10% value, more precisely between 0%–50% stress relaxation, leads to approximately a 22.6% decrease in the ultimate load for the activated beam. Similarly, this change causes approximately a 22.8% decrease in the yielding load. In both cases, the mid-span deflection and the SMA strain at concrete crushing slightly increase with an increasing stress relaxation percentage, around 15.2% for mid-span deflection and 17.1% for ultimate SMA strain. Lastly, a global sensitivity analysis was conducted via sparse polynomial chaos expansions-based (PCE) Sobol' indices. To this end, the uncertainty quantification framework Uqlab [53] was employed. A PCE-based metamodel was derived as a surrogate of the CSA script. Subsequently, the computation of the Sobol' indices follows by post-processing the coefficients of the PCE-model [54]. The results are presented in Fig. 22. The analysis considered the three input parameters, namely  $f_{ck}$  (concrete compressive strength), SMA area, and concrete Young's modulus, to investigate their effects on the output parameters, including ultimate load, mid-span deflection, and SMA strain at concrete crushing. The first-order

Sobol' indices indicate the direct influence of the input parameters on the outcome, clearly demonstrating that the most important parameter for all three output parameters is the concrete compressive strength. The SMA area also has a considerable impact on all three outputs, while the effect of concrete Young's modulus is very low to inexistent.

The total Sobol' indices demonstrate the effect of each input parameter when combined with other inputs. Once again, the concrete compressive strength comes out as the most crucial parameter for all three outputs. Unlike the first-order indices, the mid-span deflection at failure appears to be affected by the SMA cross-sectional area, when combined with other parameters (likely  $f_{ck}$ ).

## 5. Conclusions

The long-term behavior and structural response of RC beams strengthened with NSM Fe-SMA strips were investigated under sustained loading and 8 years of natural environmental exposure. A CSA algorithm was utilized to accurately simulate the bending response of the beams and to assess the effects of various parameters on the structural behavior. The following key conclusions can be deduced from the findings:

- The activated Fe-SMA strips showed a significant contribution to reducing mid-span deflections. Instantaneous mid-span deflections caused by sustained loading was 41% lower (7.3 mm versus 4.3 mm) and the long-term deflections were 24% lower (13.6 mm and 10.2 mm) for the activated beam.
- Sustained loading and environmental exposure induced time-dependent effects, such as concrete creeping and shrinkage, significantly influenced the mid-span deflection of the beams over the long-term, with approximately 55% impact on the total mid-span deflection. Concrete creep and shrinkage models based on the fib Model Code 2020 showed good agreement with the measured data.
- Despite significant irreversible mid-span deflections due to concrete creeping and cracking after long-term exposure and sustained loading, no signs of capacity reduction was observed from the four-point bending experiments, when compared to the unexposed beams that were subject to the same loading conditions. Bending response of the beams was well-reproduced by the CSA, demonstrating that long-term effects such as concrete creeping and SMA relaxation can be integrated within the conventional formulation to accurately predict cracking, yielding and ultimate

loads, as well as deflections. This implies that the methods used herein can be employed for both post-failure diagnosis and actual condition prognosis.

- Conducted parametric study and global sensitivity analysis revealed that the concrete compressive strength played a dominant role in influencing the ultimate load, mid-span deflection, and ultimate Fe-SMA strain at concrete crushing. The Fe-SMA cross-sectional area and Fe-SMA relaxation also had a notable effect on these outputs. However, the effect of concrete Young's modulus was relatively low.

Overall, the results demonstrate a satisfactory long-term durability of Fe-SMA as an NSM reinforcement, the effectiveness of CSA in analyzing the long-term behavior of the tested beams and the importance of considering time-dependent effects for accurate structural predictions.

### CRedit authorship contribution statement

**Yunus Emre Harmanci:** Writing – review & editing, Writing – original draft, Visualization, Validation, Software, Methodology, Investigation, Formal analysis. **Christoph Czaderski:** Writing – review & editing, Writing – original draft, Validation, Supervision, Methodology, Conceptualization. **Moslem Shahverdi:** Writing – review & editing, Writing – original draft, Validation, Supervision, Project administration, Methodology, Investigation.

### Declaration of competing interest

The authors declare that they have no known competing financial interests or personal relationships that could have appeared to influence the work reported in this paper.

### Data availability

Data will be made available on request.

### References

- [1] H. Martin-Sanz, E. Chatzi, E. Brühwiler, The use of ultra high performance fibre reinforced cement-based composites in rehabilitation projects: A review, in: 9th International Conference on Fracture Mechanics of Concrete and Concrete Structures, 2016, pp. 1–12.
- [2] J.G. Teng, J.F. Chen, S.T. Smith, L. Lam, Behaviour and strength of FRP-strengthened RC structures: A state-of-the-art review, *Proc. Inst. Civil Eng.-Struct. Build.* 156 (1) (2003) 51–62.
- [3] S.S. Zhang, T. Yu, G.M. Chen, Reinforced concrete beams strengthened in flexure with near-surface mounted (NSM) CFRP strips: Current status and research needs, *Composites B* 131 (2017) 30–42.
- [4] M. Badawi, K. Soudki, Flexural strengthening of RC beams with prestressed NSM CFRP rods—experimental and analytical investigation, *Constr. Build. Mater.* 23 (10) (2009) 3292–3300.
- [5] M. Motavalli, C. Czaderski, K. Pfyl-Lang, Prestressed CFRP for strengthening of reinforced concrete structures: Recent developments at Empa, Switzerland, *J. Compos. Constr.* 15 (2) (2011) 194–205.
- [6] M.A. Badawi, Monotonic and Fatigue Flexural Behaviour of RC Beams Strengthened with Prestressed NSM CFRP Rods (Ph.D. thesis), University of Waterloo, 2007.
- [7] A. Hajishahemi, D. Mostofinejad, M. Azhari, Investigation of RC beams strengthened with prestressed NSM CFRP laminates, *J. Compos. Constr.* 15 (6) (2011) 887–895.
- [8] M.M. Hosseini, S.J. Dias, J.A. Barros, Effectiveness of prestressed NSM CFRP laminates for the flexural strengthening of RC slabs, *Compos. Struct.* 111 (2014) 249–258.
- [9] F. Oudah, R. El-Hacha, Fatigue behavior of RC beams strengthened with prestressed NSM CFRP rods, *Compos. Struct.* 94 (4) (2012) 1333–1342.
- [10] M. Shahverdi, C. Czaderski, M. Motavalli, Iron-based shape memory alloys for prestressed near-surface mounted strengthening of reinforced concrete beams, *Constr. Build. Mater.* 112 (2016) 28–38.
- [11] L. Janke, C. Czaderski, M. Motavalli, J. Ruth, Applications of shape memory alloys in civil engineering structures—Overview, limits and new ideas, *Mater. Struct.* 38 (2005) 578–592.
- [12] B. Schranz, C. Czaderski, M. Shahverdi, J. Michels, T. Vogel, M. Motavalli, Ribbed iron-based shape memory alloy bars for pre-stressed strengthening applications, in: International Association for Bridge and Structural Engineering Symposium, Guimaraes, Portugal, 2019.
- [13] Y. Yang, A. Arabi-Hashemi, C. Leinenbach, M. Shahverdi, Influence of thermal treatment conditions on recovery stress formation in an FeMnSi-SMA, *Mater. Sci. Eng. A* 802 (2021) 140694.
- [14] Y. Yang, M. Breveglieri, M. Shahverdi, Effect of phase changes on the axial modulus of an FeMnSi-shape memory alloy, *Materials* 14 (17) (2021) 4815.
- [15] M. Shahverdi, S. Raza, E. Ghafoori, C. Czaderski, J. Michels, M. Motavalli, Recent advancements in development and application of an iron-based shape memory alloy at Empa, *Chimia* 76 (3) (2022) 242.
- [16] Y. Yang, C. Leinenbach, M. Shahverdi, Simulation and experimental characterization of VC precipitation and recovery stress formation in an FeMnSi-based shape memory alloy, *J. Alloys Compd.* 940 (2023) 168856.
- [17] B. Schranz, C. Czaderski, T. Vogel, M. Shahverdi, Bond investigations of pre-stressed, near-surface-mounted, ribbed memory-steel bars with full bond length, *Mater. Des.* 196 (2020) 109145.
- [18] B. Schranz, C. Czaderski, T. Vogel, M. Shahverdi, Bond behaviour of ribbed near-surface-mounted iron-based shape memory alloy bars with short bond lengths, *Mater. Des.* 191 (2020) 108647.
- [19] B. Schranz, M.F. Nunes, C. Czaderski, M. Shahverdi, Fibre optic strain measurements for bond modelling of prestressed near-surface-mounted iron-based shape memory alloy bars, *Constr. Build. Mater.* 288 (2021) 123102.
- [20] S. Raza, J. Michels, B. Schranz, M. Shahverdi, Anchorage behavior of Fe-SMA rebars post-installed into concrete, *Eng. Struct.* 272 (2022) 114960.
- [21] Z. Liu, Z. Dong, Y. Sun, H. Zhu, G. Wu, C. Sun, C.-K. Soh, Effect of resistive heating on the bond properties between iron-based shape memory bars and cement mortar, *J. Build. Eng.* 66 (2023) 105895.
- [22] H. Rojob, R. El-Hacha, Self-prestressing using iron-based shape memory alloy for flexural strengthening of reinforced concrete beams, *ACI Struct. J.* 114 (2) (2017) 523.
- [23] H. Rojob, R. El-Hacha, Fatigue performance of RC beams strengthened with self-prestressed iron-based shape memory alloys, *Eng. Struct.* 168 (2018) 35–43.
- [24] K. Hong, S. Lee, Y. Yeon, K. Jung, Flexural response of reinforced concrete beams strengthened with near-surface-mounted Fe-based shape-memory alloy strips, *Int. J. Concr. Struct. Mater.* 12 (1) (2018) 1–13.
- [25] B. Schranz, J. Michels, C. Czaderski, M. Motavalli, T. Vogel, M. Shahverdi, Strengthening and prestressing of bridge decks with ribbed iron-based shape memory alloy bars, *Eng. Struct.* 241 (2021) 112467.
- [26] C. Czaderski, M. Shahverdi, J. Michels, Iron based shape memory alloys as shear reinforcement for bridge girders, *Constr. Build. Mater.* 274 (2021) 121793.
- [27] R.A. Hawileh, Nonlinear finite element modeling of RC beams strengthened with NSM FRP rods, *Constr. Build. Mater.* 27 (1) (2012) 461–471.
- [28] H.Y. Omran, R. El-Hacha, Nonlinear 3D finite element modeling of RC beams strengthened with prestressed NSM-CFRP strips, *Constr. Build. Mater.* 31 (2012) 74–85.
- [29] H. Rojob, R. El-Hacha, Numerical investigation of the flexural performance of RC beam strengthened with iron-based shape memory alloys bar, in: Proceedings of the 27th Biennial National Conference of the Concrete Institute of Australia in Conjunction with the 69th RILEM Week. Concrete, 2015, pp. 1–9.
- [30] L.-Z. Yao, G. Wu, Nonlinear 2D finite-element modeling of RC beams strengthened with prestressed NSM CFRP reinforcement, *J. Compos. Constr.* 20 (4) (2016) 04016008.
- [31] N. Dolatabadi, M. Shahverdi, M. Ghassemieh, M. Motavalli, RC structures strengthened by an iron-based shape memory alloy embedded in a shotcrete layer—Nonlinear finite element modeling, *Materials* 13 (23) (2020) 5504.
- [32] Y.-M. Yeon, K.-N. Hong, S. Lee, S.-W. Ji, Numerical study of RC beams strengthened with Fe-based shape memory alloy strips using the NSM method, *Appl. Sci.* 11 (15) (2021) 6809.
- [33] H. Darvish, M. Shahverdi, M. Ghassemieh, Investigation of the effect of design parameters on the behavior of RC beams reinforced with shape memory alloys, *Modares Civ. Eng. J.* 22 (5) (2022).
- [34] J. Michels, M. Shahverdi, C. Czaderski, Flexural strengthening of structural concrete with iron-based shape memory alloy strips, *Struct. Concr.* 19 (3) (2018) 876–891.
- [35] B. Schranz, J. Michels, M. Shahverdi, C. Czaderski, Strengthening of concrete structures with iron-based shape memory alloy elements: Case studies, in: 5th SMAR Conference, Potsdam, Germany, 2019, pp. 1–8.
- [36] M. Shahverdi, C. Czaderski, J. Michels, Memory steel” for shear reinforcement of concrete structures, in: SMAR 2019, 2019, pp. 1–8.
- [37] M. Rezapour, M. Ghassemieh, M. Motavalli, M. Shahverdi, Numerical modeling of unreinforced masonry walls strengthened with Fe-based shape memory alloy strips, *Materials* 14 (11) (2021) 2961.
- [38] S. Raza, R. Widmann, J. Michels, M.S. Saidi, M. Motavalli, M. Shahverdi, Self-centering technique for existing concrete bridge columns using prestressed iron-based shape memory alloy reinforcement, *Eng. Struct.* 294 (2023) 116799.
- [39] J. Michels, M. Shahverdi, C. Czaderski, R. El-Hacha, Mechanical performance of iron-based shape-memory alloy ribbed bars for concrete prestressing, *ACI Mater. J.* 115 (6) (2018).

- [40] H. Rojob, R. El-Hacha, Performance of RC beams strengthened with self-prestressed Fe-SMA bars exposed to freeze-thaw cycles and sustained load, *Eng. Struct.* 169 (2018) 107–118.
- [41] M. Shahverdi, C. Czaderski, Long-term behavior of reinforced concrete beams strengthened by iron-based shape memory alloy strips, *Proc. SMAR* (2019).
- [42] Y.E. Harmanci, J. Michels, C. Czaderski, M. Motavalli, Calculation technique for externally unbonded CFRP strips in structural concrete retrofitting, *J. Eng. Mech.* 142 (6) (2016) 04016026.
- [43] B. Schranz, P.-R. Wagner, C. Czaderski, M. Shahverdi, Fibre optic measurements and model uncertainty quantification for Fe-SMA strengthened concrete structures, *Eng. Struct.* 256 (2022) 114005.
- [44] M. Shahverdi, J. Michels, C. Czaderski, M. Motavalli, Iron-based shape memory alloy strips for strengthening RC members: Material behavior and characterization, *Constr. Build. Mater.* 173 (2018) 586–599.
- [45] S.N. E. N. 13791, Bewertung der Druckfestigkeit von Beton in Bauwerken und in Bauwerksteilen (in German), European Standards, 2019.
- [46] F.I. du Béton (fib), FIB Model Code 2020 for Concrete Structures, Ernst & Sohn, Berlin, 2020.
- [47] J. Sena-Cruz, J. Michels, Y.E. Harmanci, L. Correia, Flexural strengthening of RC slabs with prestressed CFRP strips using different anchorage systems, *Polymers* 7 (10) (2015) 2100–2118.
- [48] J. Michels, M. Staśkiewicz, C. Czaderski, R. Kotynia, Y.E. Harmanci, M. Motavalli, Prestressed CFRP strips for concrete bridge girder retrofitting: Application and static loading test, *J. Bridge Eng.* 21 (5) (2016) 04016003.
- [49] J. Michels, D. Zwicky, J. Scherer, Y.E. Harmanci, M. Motavalli, Structural strengthening of concrete with fiber reinforced cementitious matrix (FRCM) at ambient and elevated temperature—Recent investigations in Switzerland, *Adv. Struct. Eng.* 17 (12) (2014) 1785–1799.
- [50] S. Matthys, Structural Behaviour and Design of Concrete Members Strengthened with Externally Bonded FRP Reinforcement (Ph.D. thesis), Ghent University, 2000.
- [51] B. Sudret, Global sensitivity analysis using polynomial chaos expansions, *Reliab. Eng. Syst. Saf.* 93 (7) (2008) 964–979.
- [52] J.-K. Kim, S.-T. Yi, C.-K. Park, S.-H. Eo, Size effect on compressive strength of plain and spirally reinforced concrete cylinders, *Struct. J.* 96 (1) (1999) 88–94.
- [53] S. Marelli, B. Sudret, UQLab: A framework for uncertainty quantification in MATLAB, in: *Proc. 2nd Int. Conf. on Vulnerability, Risk Analysis and Management, ICVRAM2014*, Liverpool, United Kingdom, 2014.
- [54] R. Schöbi, B. Sudret, PCE-based imprecise sobol'indices, in: *Proceedings of the 12th International Conference on Structural Safety and Reliability, ICOSSAR 2017*, TU Verlag, 2017, pp. 513–520.